ADVANCED ELECTRONIC MATERIALS
Open Access
www.advelectronicmat.de

Composition-Dependent Ferroelectricity of $LuFeO_3$ Orthoferrite Thin Films

*Eunsoo Cho, Konstantin Klyukin, Tingyu Su, Allison Kaczmarek, and Caroline A. Ross**

This work characterizes the structural, magnetic, and ferroelectric properties of epitaxial $LuFeO_3$ orthoferrite thin films with different Lu/Fe ratios. $LuFeO_3$ thin films are grown by pulsed laser deposition on $SrTiO_3$ substrates with Lu/Fe ratio ranging from 0.6 to 1.5. $LuFeO_3$ is antiferromagnetic with a weak canted moment perpendicular to the film plane. Piezoresponse force microscopy imaging and switching spectroscopy reveal room temperature ferroelectricity in Lu-rich and Fe-rich films, whereas the stoichiometric film shows little polarization. Ferroelectricity in Lu-rich films is present for a range of deposition conditions and crystallographic orientations. Positive-up-negative-down ferroelectric measurements on a Lu-rich film yield ≈13 $\mu C\ cm^{-2}$ of switchable polarization, although the film also shows electrical leakage. The ferroelectric response is attributed to antisite defects analogous to that of Y-rich $YFeO_3$, yielding multiferroicity via defect engineering in a rare earth orthoferrite.

1. Introduction

Oxides of rare earths (R) and iron can form a range of crystal structures depending on their R to Fe ratio, including RFe_2O_4, $R_3Fe_5O_{12}$ (rare earth iron garnet), $R_2Fe_3O_7$, orthorhombic $RFeO_3$, and hexagonal $RFeO_3$. These materials exhibit a diverse variety of useful properties such as magnetism,[1] ferroelectricity,[2] multiferroicity,[3] magnetoresistance,[4] magnetooptical activity,[5] and catalytic activity.[6] The electrical, magnetic, optical, and transport properties of these and other complex oxides are strongly influenced by point defects resulting from a nonideal cation stoichiometry.[7–12] Such point defects can be present in much higher concentrations in thin films compared to bulk, due to epitaxial stabilization of a crystal structure with a composition deviating from bulk.[11,12]

The orthoferrites ($RFeO_3$) are perovskite-derived structures in which tilting of the Fe octahedra yields an orthorhombic lattice with four formula units (f.u.) per unit cell.[13] Fe^{3+} cations are coupled antiferromagnetically with Néel temperature $T_N \approx 640$ K. The Dzyaloshinskii–Moriya interaction (DMI) between neighboring Fe^{3+} leads to a small canting angle and a net moment ≈0.05 μ_B per f.u. at room temperature. The antiferromagnetic configuration of Fe^{3+} (Γ_1, Γ_2, or Γ_4 in Bertaut notation) and the magnetic transition temperatures between different antiferromagnetic states varies with the rare earth. For a nonmagnetic R^{3+} such as Lu^{3+}, the configuration remains Γ_4 ($G_xA_yF_z$, i.e., G-type antiferromagnet with spins oriented along x, with secondary A-type antiferromagnetic arrangement along y, and a net moment along z) from 0 K up to T_N.[14,15] Some orthoferrites can exhibit multiferroicity at cryogenic temperatures when R^{3+} ions are magnetically ordered.[16] The mechanism for such ferroelectricity is the exchange interaction between R^{3+} and Fe^{3+}, which leads to ionic displacement, breaks the symmetry, and thus leads to polarization on the order of 0.1 $\mu C\ cm^{-2}$.[16,17]

Introducing room-temperature ferroelectricity into antiferromagnetic orthoferrites is an appealing strategy to expand the range of room temperature multiferroic materials. The most widely studied multiferroic is $BiFeO_3$ (BFO), which is a rhombohedral or tetragonal structure. Its ferroelectricity is derived primarily from the Bi^{3+} lone pairs and exhibits a high ferroelectric Curie temperature ($T_C = 1103$ K).[18] As in the rare earth orthoferrites, the magnetism in BFO arises from the canting of antiferromagnetically ordered Fe^{3+} spins with $T_N = 643$ K. Rare earth orthoferrites lack the lone pairs of BFO, and the centrosymmetric orthorhombic space group (*Pbnm*) prohibits ferroelectricity. However, Y_{Fe} antisite defects in Y-rich yttrium orthoferrite $YFeO_3$ (YFO) thin films bring about a noncentrosymmetric structural distortion and induce ferroelectric polarization of ≈10 $\mu C\ cm^{-2}$ at room temperature.[19–21] According to first principles calculations, such an antisite defect mechanism is expected to be applicable in other rare earth rich orthoferrites, with the polarization increasing with decreasing ionic radius of R^{3+}; $LuFeO_3$ (LFO) lies at the higher end of

---

E. Cho, K. Klyukin, A. Kaczmarek, C. A. Ross
Department of Materials Science and Engineering
Massachusetts Institute of Technology
Cambridge, MA 02139, USA
E-mail: caross@mit.edu

K. Klyukin
Department of Materials Engineering
Auburn University
Auburn, AL 36849, USA

T. Su
Department of Mechanical Engineering
Massachusetts Institute of Technology
Cambridge, MA 02139, USA

The ORCID identification number(s) for the author(s) of this article can be found under https://doi.org/10.1002/aelm.202300059.

DOI: 10.1002/aelm.202300059

predicted polarization.[19] It is therefore of interest to investigate the effect of antisite defects on the ferroic properties of LFO.

Previous studies of the stoichiometric orthoferrite LFO report that remnant polarization (P_r) ranges from several nC cm^{-2} (polycrystalline LFO)[22–24] up to ≈15 μC cm^{-2} (thin film LFO)[25] at room temperature. The ferroelectricity in polycrystalline LFO was first explained by exchange striction at magnetic domain walls,[22] or by charge disproportionation from increased covalency,[24] and the higher polarization in thin films was ascribed to the tetragonally strained structure with an out-of-plane to in-plane lattice parameter ratio of 1.045.[25] Polycrystalline $Y_{1-x}Lu_xFeO_3$ also showed unsaturated polarization versus electric field (P–E) loops, and the hysteresis was attributed to symmetry breaking from the mixing of Lu and Y ions.[26] A metastable hexagonal LFO phase was found to be ferroelectric due to its noncentrosymmetric crystal structure, with T_C = 1020 K and P_r up to ≈10 μC cm^{-2} at room temperature.[27–29] Both orthorhombic and hexagonal LFO phases have been grown in the form of thin films using pulsed laser deposition (PLD),[25,27,30] radio frequency magnetron sputtering,[31,32] or molecular beam epitaxy.[28] When the two phases are grown together, the film can show multiferroicity with a magnetization of ≈0.24 μ_B per f.u. from the orthorhombic phase and a polarization of ≈5 μC cm^{-2} from the hexagonal phase.[29]

Orthorhombic LFO is a good candidate for defect engineered multiferroic material because the magnetic order persists above room temperature (T_N = 623 K), in contrast to hexagonal LFO with T_N = 155 K.[28] However, so far, orthorhombic LFO has not received as much attention as hexagonal LFO, and the stoichiometry range this material can tolerate as a single-phase film has not been explored.

Here, we grow epitaxial orthorhombic LFO thin films with Lu/Fe ratio varying from 0.6 to 1.5, and characterize their structural, magnetic, and ferroelectric properties at room temperature. LFO films with different orientations grown on $SrTiO_3$ (STO) form a single-phase perovskite despite their non-ideal cation stoichiometry, which in bulk would favor the formation of secondary phases. The observation of ferroelectric hysteresis by different methods (piezoresponse force microscopy (PFM), P–E loops, and positive-up-negative-down (PUND) measurements) all support the hypothesis of antisite-defect-mediated ferroelectricity in orthoferrites with nonstoichiometric R:Fe ratio.

2. Results and Discussion

LFO thin films with Lu/Fe ratios of 0.6, 0.8, 1.0, 1.2, and 1.5 were grown on (001)-oriented STO (insulating) and Nb-doped STO (NSTO, conductive) substrates with a = 3.905 Å (**Figure 1**a). There were no secondary phases observed in the wide angle range X-ray diffraction (XRD) scans (15°–80°, Figure S1, Supporting Information) for any of the films, despite the fact that according to the Lu–Fe–O ternary phase diagram,[33] LFO does not accommodate significant excess Lu or Fe, instead forms additional phases such as $LuFe_2O_4$, $Lu_3Fe_5O_{12}$, $Lu_2Fe_3O_7$, hexagonal $LuFeO_3$, or binary oxides when Lu/Fe differs from 1.0. Due to the ionic radius difference between Lu^{3+} (86 pm) and Fe^{3+} (60 pm), as the film becomes Lu-rich, the XRD peak position 2θ of $(002)_p$ (p denotes the pseudocubic notation) moves to a lower angle and the out-of-plane lattice parameter c_p increases from 3.789 Å (Lu/Fe = 0.6), 3.793 Å (Lu/Fe = 0.8), 3.800 Å (Lu/Fe = 1.0), 3.820 Å (Lu/Fe = 1.2), to 3.846 Å (Lu/Fe = 1.5). The monotonic trend in the peak position differs from that observed in YFO, when the 2θ angle increased then decreased as the film composition moved from Y-rich to Fe-rich.[19]

XRD of Lu/Fe = 1.2 films grown at different oxygen partial pressure (P_{O2}) is shown in Figure 1b. The 2θ angle shifts to a higher value as the pressure increases, consistent with a reduction in the oxygen vacancy (V_O) concentration with increasing oxygen pressure. Lu/Fe = 1.2 films were also grown on (111) and (110)-oriented NSTO substrates (Figure S1, Supporting Information), and similar to the (100)-oriented substrates, only reflections arising from epitaxial perovskite LFO are observed. In Figure 1c, Lu/Fe = 1.2 films were grown on different substrates, $LaAlO_3$ (LAO) with a_p = 3.788 Å and $(LaAlO_3)_{0.3}$–$(SrAl_{0.5}Ta_{0.5}O_3)_{0.7}$ (LSAT) with a_p = 3.868 Å. Film 2θ positions show minimal change with respect to the substrate. This is different from the behavior of YFO where the peak position shifted for different substrates.[19]

The reciprocal space mapping (RSM) data of the $(103)_p$ reflection, shown in Figure 1d for Lu/Fe = 1.2 and Figure 1e for Lu/Fe = 1.0, indicates cube-on-cube epitaxy of the LFO on STO substrates. Although the crystal quality of Fe-rich films was not good enough to produce a peak in RSM (Figure 1f), the peak positions of the other films indicate in-plane incoherency. In-plane pseudocubic lattice parameters extracted from RSM are 4.017 and 3.987 Å for Lu/Fe = 1.2 and Lu/Fe = 1.0, respectively, compared with out-of-plane lattice pseudocubic lattice parameters 3.820 and 3.800 Å. Unit cell volumes are greater by ≈10% compared to bulk LFO, which is consistent with a greater oxygen deficiency in thin films versus bulk. In contrast, the YFO film unit cell volume was only 1% greater than that of bulk YFO.[19] Atomic force microscope (AFM) images of the Lu/Fe = 1.2 film, Figure 1g, shows island-like roughening common to PLD-grown films; the root mean square roughness is 0.460 nm for a ≈30 nm thick film.

Figure 2 is the magnetic hysteresis loop of the Lu/Fe = 1.2 film measured at room temperature, with the magnetic field applied in both out-of-plane (OP) and in-plane (IP) directions. The out-of-plane moment saturates at around 1 T with a saturation magnetization M_s ≈0.8 kA m^{-1}, which is about an order of magnitude lower than that of bulk.[14] However, the in-plane moment does not saturate up to 2 T. This suggests that the orthorhombic c axis in *Pbnm* notation is perpendicular to the film because the weak ferromagnetism from DMI is along the c axis. Based on the magnetic properties and structural analysis, we conclude that the epitaxy of LFO films on perovskite substrates can be represented as Figure 1h. The orthorhombic a and b axes lie in-plane, 45° rotated with respect to the pseudocubic unit cell, and the orthorhombic c axis lies out-of-plane with lattice parameter = $2c_p$.

In order to characterize the ferroelectric properties, we performed switching spectroscopy via PFM (SS-PFM) and used the PFM tip to write polarization patterns on LFO thin films. **Figure 3**a,b,c shows the SS-PFM amplitude and phase hysteresis of LFO films with Lu/Fe of 1.2, 1.0, and 0.8, along with the remnant polarization after writing a "box-in-box" pattern, i.e., polarizing a 1 μm square region at −8 V tip bias then a

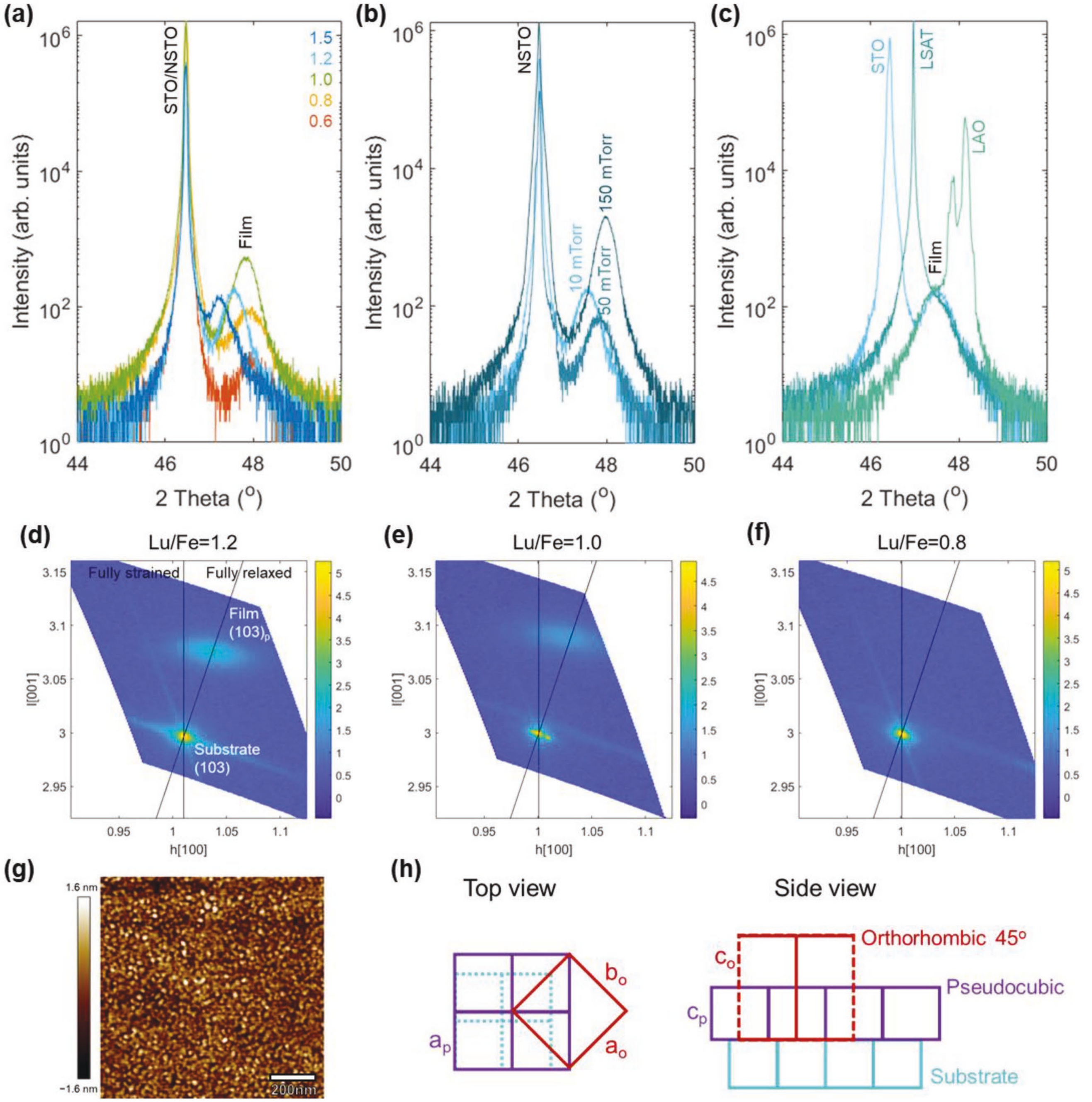

Figure 1. XRD around the substrate (002) and film $(002)_p$ reflections for samples with a) different Lu/Fe ratio, b) different P_{O2} during growth, and c) different substrates. Reciprocal space mapping around the (103) substrate and $(103)_p$ film reflections for Lu/Fe = d) 1.2, e) 1.0, and f) 0.8 films on STO. g) AFM scan of Lu/Fe = 1.2 film. h) Epitaxy scheme of LFO growth on perovskite substrates (o stands for orthorhombic and p stands for pseudocubic).

smaller square region at +8 V. The Lu-rich film shows ferroelectricity which can be interpreted using the antisite defect mechanism.[19] SS-PFM hysteresis was observed in several Lu-rich films grown with different orientations or at different P_{O2} (Figure 3d,e). Moreover, films grown with top and bottom conductive $SrRuO_3$ (SRO) layers also exhibit ferroelectric switching (Figure S2a–c, Supporting Information). With the SRO top layer, the tip is in contact with a conductive layer which rules out surface charging artifacts of PFM.

All the Lu-rich, stoichiometric, and Fe-rich LFO films showed hysteretic behavior in PFM, although the amplitude of SS-PFM and the phase contrast produced by domain writing is much smaller for Lu/Fe = 1.0. This behavior differs from that of YFO films where the ferroelectric response was limited to Y-rich compositions. The ferroelectricity in Y-rich YFO was explained by antisite defects Y_{Fe} on the octahedral sites, which lower the symmetry to a noncentrosymmetric *R3c* structure.[19] If the same mechanism exists in LFO, it can account for the ferroelectric response in the Lu-rich composition. For the film with Lu/Fe = 1.0, we hypothesize that the (weaker) ferroelectricity may also be caused by antisite defects, even though the composition would suggest that few such defects need be present. The XRD peak intensities provide support for the presence of antisite defects (i.e., both $\mathrm{Lu_{Fe}}$ and $\mathrm{Fe_{Lu}}$) in the film with Lu/Fe = 1.0. Using a pseudocubic ABO_3 perovskite unit cell, the structure factors F_{hkl} of the (001) and (002) reflections are $F_{001} = f_A - f_B - f_O$ and $F_{002} = f_A + f_B + 3f_O$. The peak intensities I_{hkl} are then

$$I_{001} \propto f_A^2 + f_B^2 + f_O^2 - 2f_Af_B - 2f_Af_O + 2f_Bf_O \qquad (1)$$

$$I_{002} \propto f_A^2 + f_B^2 + 9f_O^2 + 2f_Af_B + 6f_Af_O + 6f_Bf_O \qquad (2)$$

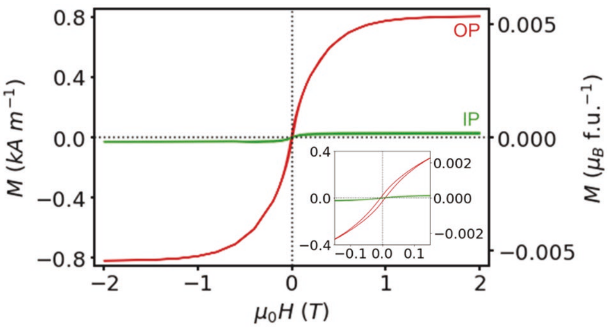

Figure 2. Magnetic hysteresis loop of Lu/Fe = 1.2 film measured at 300 K. The inset shows the low-field regime.

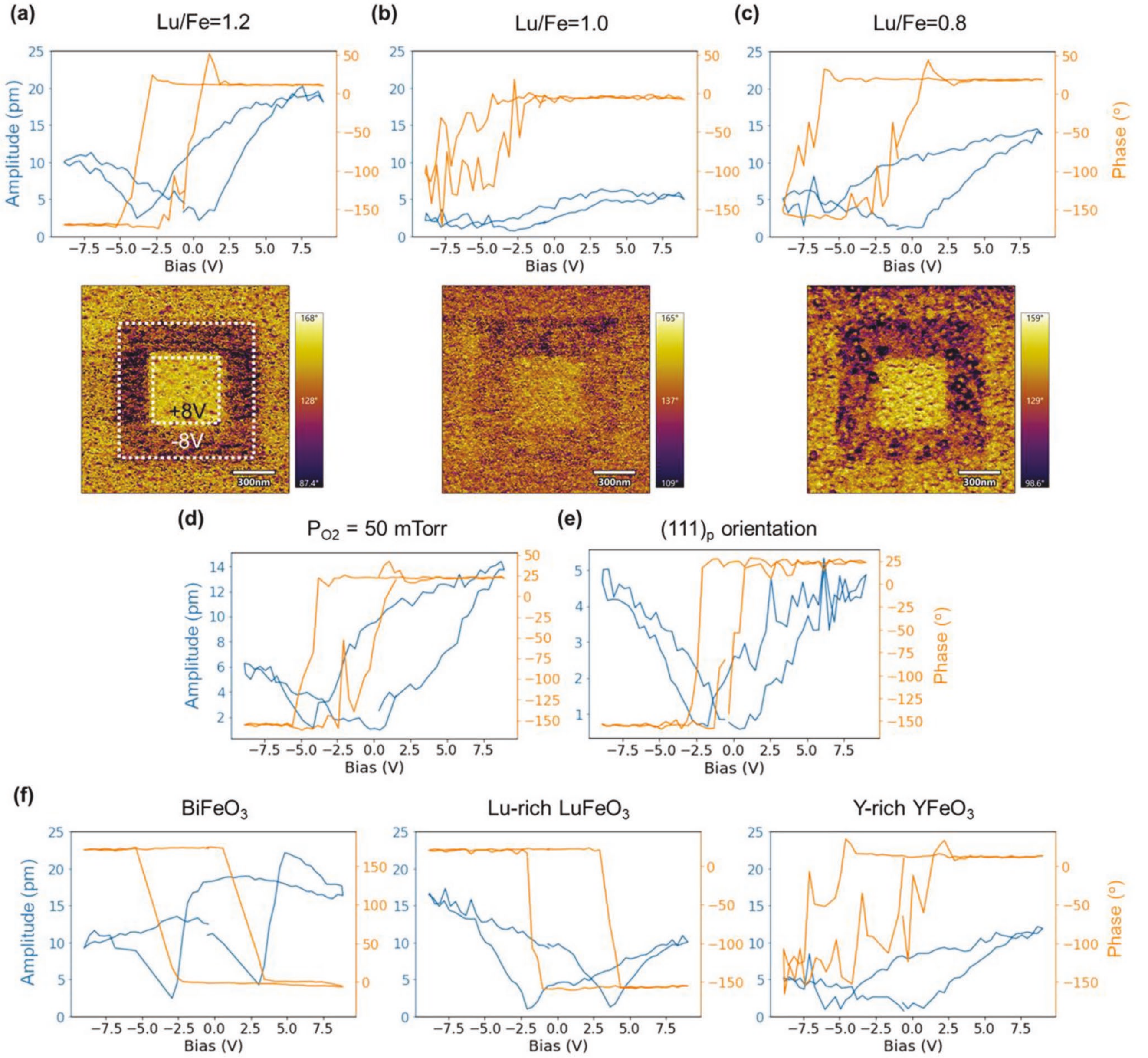

Figure 3. SS-PFM hysteresis and phase contrast after writing domain structures with a bias of ± 8 V on $(001)_p$-oriented LFO films with Lu/Fe stoichiometry of a) 1.2, b) 1.0, and c) 0.8. SS-PFM of Lu/Fe = 1.2 film grown at different conditions, d) $P_{O2} = 50$ mTorr and e) in $(111)_p$ orientation. f) SS-PFM results of different orthoferrites performed with the same tip. BFO, LFO, and YFO films are 23, 33, and 40 nm, respectively.

Table 1. Formation energies (ΔE) per orthorhombic $\sqrt{2} \times \sqrt{2} \times 1$ supercell (in-plane lattice = 7.810 Å) of different point defects in LFO. ΔE was calculated with respect to the defect-free LFO strained on STO as the ground state.

Defect	V_O (IP)	V_O (OP)	V_{Lu}	V_{Fe}	Lu_{Fe}	Fe_{Lu}	Lu_{Fe}+Fe_{Lu}
ΔE [eV]	4.74	5.10	5.57	6.97	2.89	–1.43	1.32

The (θ-dependent) values of f_A and f_B are modified by the presence of antisites, Fe_{Lu} on the A sites and Lu_{Fe} on the B sites. By weighting f_A and f_B with the antisite concentration (i.e., $f_A = f_{Lu} \times$ (fraction of Lu sites occupied by Lu) + $f_{Fe} \times$ (fraction of Lu sites occupied by Fe), etc.), we calculate the intensity ratio $IR = I(001)/I(002)$ shown as a contour plot in Figure S3 in the Supporting Information. For the case with minimum antisites, i.e., none for Lu/Fe = 1.0, and Lu_{Fe} only for excess Lu, we find that $IR(\text{Lu/Fe} = 1.0) = \beta\, IR(\text{Lu/Fe} = 1.2)$ where $\beta = 1.4$. However, the experimental data gives a ratio of $\beta = 1.2$. This is inconsistent with zero defects in the film with Lu/Fe = 1.0 and instead suggests the presence of Lu_{Fe} and Fe_{Lu} according to Figure S3 in the Supporting Information. This analysis was not applied to the data from the Fe-rich films because the poorer crystallinity itself lowers the peak intensities (both $(103)_p$ in RSM and $(003)_p$ in XRD are absent), and excess Fe also leads to other defects, such as dislocations or cation vacancies observed in Fe-rich YFO which may also occur in Fe-rich LFO.

The feasibility of finding both Lu_{Fe} and Fe_{Lu} antisite defects in LFO films is supported by density functional theory (DFT) calculations. The defect energies are shown in **Table 1**, which were calculated using the equation

$$\Delta E = E(\text{defective LFO}) + (\mu \text{ of defect species}) - E(\text{defect} - \text{free LFO}) \quad (3)$$

under the assumption of Fe-rich and O-rich conditions and with in-plane pseudocubic lattice parameter of 3.905 Å (crystal structures are shown in Figure S4 in the Supporting Information). While the formation energies of cation or anion vacancies range from 4.74 to 6.97 eV, the formation of antisite defects is energetically more favorable, suggesting abundant distribution of these defects in thin films. This highlights the feasibility of antisite defect formation in LFO, which may explain the presence of ferroelectricity in LFO of various compositions including Lu/Fe = 1.0 via the mechanism presented for Y-rich YFO.[19] It is worth noting that a negative formation energy of the Fe_{Lu} defect is associated with intrinsic instability of bulk orthorhombic phase LFO. In agreement with ref. [33], the thermodynamic phase diagram (Figure S5, Supporting Information) constructed based on the calculated enthalpies of Fe_2O_3, Lu_2O_3, and LFO oxides indicates that the orthorhombic LFO structure is not stable, consistent with the depiction as a point in the ternary phase diagram, and can be stabilized by epitaxial growth.

In order to qualitatively compare the magnitude of polarization among different orthoferrites, SS-PFM was performed using the same tip on Lu-rich LFO, Y-rich YFO, and BFO, and the results are shown in Figure 3f. The PFM amplitude is the highest in BFO, followed by LFO, and YFO. In a ferroelectric material with *4mm* symmetry, the piezoelectric coefficient d_{33} and polarization P_3 are related by $d_{33} = 2\varepsilon_0\varepsilon_{33}Q_{3333}P_3$ where ε_0 is the permittivity of vacuum, ε_{33} is the relative permittivity, and Q_{3333} the electrostrictive coefficient,[34] therefore we expect the PFM amplitude to be proportional to the polarization. We also note that perovskite ferroelectrics tend to show higher PFM amplitude when they are thicker.[35–37] Assuming LFO and YFO have similar ε_{33} and Q_{3333} and considering that the LFO sample is thinner than YFO, the measurements of PFM amplitude, which is proportional to d_{33}, implies that LFO has a higher polarization than YFO (as predicted[19]), but lower than BFO.

P–E loop and PUND results of Lu-rich LFO with a Pt top electrode are shown in **Figure 4**a,b. In Figure 4a, a clear ferroelectric saturation feature is observed at high positive bias and switching current peaks are observed for both bias directions; however, the *P–E* loop at negative bias shows a more resistive-like behavior. Current leakage is also confirmed by the increase in the current at higher bias, similar to that observed in $Hf_{0.5}Zr_{0.5}O_2$.[38] The *P–E* loop shape indicates that the LFO has a lower resistivity compared to other ferroelectrics (i.e., $PbZr_xTi_{1-x}O_3$, PZT) and a diode-like behavior from the asymmetric electrode structure. The resistivity of LFO was 1.5×10^8 Ω cm (Figure 4c), measured by impedance spectroscopy to minimize the contribution of contact resistance. This value agrees with the resistivity calculated from the current flow at 1 V bias. The LFO resistivity is two or more orders of magnitude lower than that of PZT.[39] We attempted to increase the resistivity by using Ti^{4+} as a dopant under the assumption that LFO is a p-type conductor.[40] Although Ti was successfully incorporated in the LFO without producing any secondary phases, the resistivity decreased to ≈10^6 Ω cm, implying the leakage was due to a different mechanism.

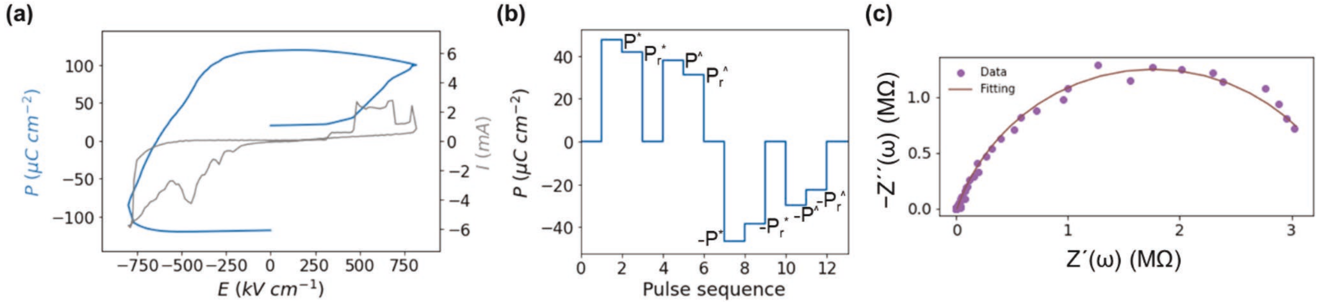

Figure 4. a) *P–E* hysteresis (10 kHz) overlaid with the measured current and b) PUND result (pulse width 1.5 ms, pulse delay 100 ms) of a 73-nm-thick Lu/Fe = 1.2 LFO/NSTO film with Pt top electrodes. c) Impedance spectroscopy measured from 1 MHz to 1 Hz (open circuit condition).

Asymmetric P–E loops (ferroelectric hysteresis for one direction of bias and resistive for the other) have been reported in BFO and PZT. V_O accumulation at the interface in BFO[41–44] caused such loops, and different diode characteristics at the interface may have contributed to asymmetry as well. We attempted to reduce the leakage and its directionality by using SRO as both top and bottom electrodes, but the asymmetry and leakage were still present as shown by the rounded hysteresis loop shape (Figure S2d, Supporting Information). This may be a result of inequivalent growth condition of the SRO, in which the bottom layer is grown directly on the substrate, whereas the top layer is grown on the strain-relaxed LFO film. These results, along with studies on BFO or PZT,[27,39] highlight the importance of process parameters in ferroelectric film growth. During P–E measurements, some electrodes exhibited capacitive behavior at first, but applying a pulse similar to or higher than the coercive field could activate the film into showing ferroelectric behavior. A similar phenomenon was observed in PZT by removing pinned domains,[45] although the mechanism for LFO may not be the same, considering that LFO is an improper ferroelectric whereas PZT (or BFO) are proper ferroelectrics. The primary order parameter for proper ferroelectric transitions is polarization, while in improper ferroelectrics, polarization is derived from other order parameters (e.g., structural distortion arising from $\mathrm{Lu_{Fe}}$).[13,27]

PUND measurements were performed to exclude parasitic contributions from the P–E hysteresis and to extract the switchable polarization of LFO. The difference between the remnant polarization from the switching pulse (P_r^*) and the nonswitching pulse ($P_r^\wedge$) is equivalent to the net switchable polarization (Q_{SW}, or $2P_r$). Q_{SW} and $-Q_{SW}$ derived from Figure 4b are 10.8 and –15.8 μC cm^{-2}, respectively, and the difference presumably rises from the asymmetric electrode configuration. The average value of 13.3 μC cm^{-2} is higher than that of Q_{SW} = 7.2 μC cm^{-2} for YFO, which is in line with the hypothesis that Lu-rich LFO would have a higher polarization than Y-rich YFO.[19] Nevertheless, high $\pm P_r^\wedge$ in the PUND measurement indicates that the leakage, which is concurrent with ferroelectric switching, is significant when the field approaches and overcomes the coercivity, and it is also consistent with the leaky behavior in the P–E loop in Figure 4a. Reducing the leakage of LFO films is necessary to improve the performance of LFO as a room temperature multiferroic material.

3. Conclusion

This study presents the structural, magnetic, and ferroelectric behavior of epitaxial LFO thin films grown using PLD, particularly revealing ferroelectricity depending on Lu/Fe stoichiometry which is attributed to an antisite-defect-mediated mechanism. The out-of-plane magnetic hysteresis of LFO films shows small canted ferromagnetism and thus corresponds to the orthorhombic c axis in $Pbnm$ notation. Using SS-PFM, particularly focusing on the Lu-rich composition with Lu/Fe = 1.2, we demonstrate room temperature ferroelectric behavior over a range of growth conditions. Moreover, we attribute the presence of ferroelectricity across all compositions to the abundance of antisite defects in LFO, which have a low formation energy according to DFT. The remnant polarization obtained from the PUND measurement is 13.3 μC cm^{-2} for Lu-rich LFO, higher than that of Y-rich YFO. However, the ferroelectric performance is limited by the low resistivity of LFO. This work realizes room temperature multiferroicity in films of an orthoferrite, LFO, and supports the model of ferroelectricity derived from antisite defect engineering in rare earth orthoferrites.

4. Experimental Section

Thin Film Growth: Epitaxial LFO films were grown by PLD using a 248 nm wavelength KrF excimer laser with a fluence of ≈2 J cm^{-2} from oxide targets prepared with two different Lu/Fe ratios, 0.6 ($\mathrm{Lu_3Fe_5O_{12}}$, the stoichiometry of garnet) and 1.4. The Lu/Fe stoichiometry of the targets and film end members were measured by wavelength dispersive spectroscopy (WDS) using a JEOL-JXA-8200 Superprobe. The Lu/Fe = 0.6 target resulted in a film with the same Lu/Fe ratio, however, the Lu/Fe = 1.4 target resulted in a film enriched in rare earth (Lu/Fe = 1.5). A similar result was also seen in the growth of Y-rich YFO from a stoichiometric YFO target.[19] The Lu/Fe ratio of the film was varied by adjusting the shot ratio between the two targets based on their growth rates to achieve the desired stoichiometry. The substrate heater temperature setpoint was 900 °C (actual substrate temperature ≈650 °C) and P_{O2} was 10–150 mTorr during growth. For comparison, YFO was grown at the same deposition conditions as LFO from an oxide target with Y/Fe = 1 resulting in a film with Y/Fe = ≈1.2, and BFO was grown in a different chamber using a Bi/Fe = 1.2 oxide target with substrate heater setpoint of 700 °C (actual substrate temperature ≈550 °C). For some samples, conductive layers of SRO were grown in situ, above and below LFO, at the same P_{O2} and temperature as LFO.

Structural, Magnetic, and Ferroelectric Characterization: Structural characterization by XRD was done using a Rigaku Smartlab high resolution diffractometer with a Cu Kα_1 (wavelength 1.5406 Å) X-ray source. RSM was performed with a Bruker D8 Discover diffractometer, also using a Cu Kα_1 source. Magnetic hysteresis was measured in a Quantum Design MPMS3 SQUID magnetometer at 300 K. AFM imaging was performed using a Bruker Dimension Icon XR scanned probe microscope, and PFM was performed using an Asylum Research Cypher VRS AFM in dual AC resonance tracking (DART) mode. Both probe microscopies were done using Pt-coated Si probes from MikroMasch (HQ:NSC18/Pt). SS-PFM data was processed with a simple harmonic oscillator model using built-in software. A Radiant Technologies Precision Premier II tester was used for P–E hysteresis and PUND pulse measurements. Prior to electrical measurements, Pt electrodes with a diameter of 200 μm were deposited by sputtering using a shadow mask, and for samples with SRO layers, the top SRO layer was patterned by photolithography (Heidelberg MLA 150) and ion milled, while the underlying SRO layer below the LFO remained continuous.

Computational Methods: DFT studies were done using the Vienna Ab initio Simulation Package (VASP).[46,47] Generalized gradient approximation (GGA) parameterized by Perdew–Burke–Ernzerhof (PBE)[48] functional was used for the exchange-correlation term. The plane-wave cutoff energy was 500 eV. The rotationally averaged Hubbard correction with an effective U_{eff} = 4 eV for Fe 3d electrons was used. Lu $5p^6 5d^1 6s^2$, Fe $3p^6 3d^7 4s^1$, and O $2s^2 2p^4$ electrons were treated as valence. Enthalpies of oxide formation and defect formation energies were adjusted, taking into account $\mathrm{O_2}$ overbinding and the use of Hubbard U correction scheme according to refs. [49] and [50], respectively. In the case of LFO, a $\sqrt{2} \times \sqrt{2} \times 1$ supercell with 8 f.u. was used with a $4 \times 4 \times 4$ Monkhorst–Pack k-point grid. For defect formation energy calculations, the structures were epitaxially strained to the lattice parameter of STO (a = 3.905 Å), but relaxed in the out-of-plane direction. The formation enthalpy of each compound was calculated by

$$\Delta H_{\mathrm{Fe_2O_3}} = E_{\mathrm{Fe_2O_3}} - 2E_{\mathrm{Fe}} - 3\mu_{\mathrm{O}} \tag{4}$$

$$\Delta H_{\mathrm{Lu_2O_3}} = E_{\mathrm{Lu_2O_3}} - 2E_{\mathrm{Lu}} - 3\mu_{\mathrm{O}} \tag{5}$$

$$\Delta H_{\mathrm{LuFeO_3}} = E_{\mathrm{LuFeO_3}} - E_{\mathrm{Lu}} - E_{\mathrm{Fe}} - 3\mu_{\mathrm{O}} \tag{6}$$

where $\mu_{\mathrm{O}} = \frac{1}{2}E_{\mathrm{O_2}}$. The formation enthalpies of Fe_2O_3, Lu_2O_3, and LFO were −8.47, −20.67, and −14.55 eV per f.u., and the choice of parameters with Fe Hubbard U correction[50] showed a good agreement with the experimental formation enthalpies of binary oxides Fe_2O_3 and Lu_2O_3.[51]

Supporting Information

Supporting Information is available from the Wiley Online Library or from the author.

Acknowledgements

The authors are grateful for guidance and assistance from Jason Tresback (Harvard CNS) on PFM characterization, Joe Evans (Radiant Technologies) on electrical characterization, Taekyong Kim (MIT EECS) on electrical characterization, and Han Gil Seo (MIT DMSE) on impedance spectroscopy. This work was supported by NSF DMR-2132623, and performed in part in the MIT.nano Characterization Facilities on the Cypher VRS enabled by DURIP award (N000142012203) and the MIT shared facilities enabled by MRSEC award DMR-1419807.

Conflict of Interest

The authors declare no conflict of interest.

Data Availability Statement

The data that support the findings of this study are available from the corresponding author upon reasonable request.

Keywords

complex oxides, defect engineering, multiferroic thin films, off-stoichiometry, orthoferrites

Received: January 30, 2023
Revised: March 27, 2023
Published online:

---

[1] E. R. Rosenberg, K. Litzius, J. M. Shaw, G. A. Riley, G. S. D. Beach, H. T. Nembach, C. A. Ross, *Adv. Electron. Mater.* **2021**, *7*, 2100452.
[2] J. De Groot, T. Mueller, R. A. Rosenberg, D. J. Keavney, Z. Islam, J. W. Kim, M. Angst, *Phys. Rev. Lett.* **2012**, *108*, 187601.
[3] Y. Tokura, S. Seki, N. Nagaosa, *Rep. Prog. Phys.* **2014**, *77*, 076501.
[4] G. R. Hoogeboom, T. Kuschel, G. E. W. Bauer, M. V. Mostovoy, A. V. Kimel, B. J. Van Wees, *Phys. Rev. B* **2021**, *103*, 134406.
[5] T. Fakhrul, S. Tazlaru, B. Khurana, L. Beran, J. Bauer, M. Vančík, A. Marchese, E. Tsotsos, M. Kučera, Y. Zhang, M. Veis, C. A. Ross, *Adv. Opt. Mater.* **2021**, *9*, 2100512.
[6] T. Arakawa, S. Tsuchi-ya, J. Shiokawa, *Mater. Res. Bull.* **1981**, *16*, 97.
[7] M. D. Scafetta, S. J. May, *Phys. Chem. Chem. Phys.* **2017**, *19*, 10371.
[8] F. M. Chiabrera, F. Baiutti, J. M. Börgers, G. F. Harrington, L. Yedra, M. O. Liedke, J. Kler, P. Nandi, J. de Dios Sirvent, J. Santiso, M. López-Haro, J. J. Calvino, S. Estradé, M. Butterling, A. Wagner, F. Peiró, R. A. De Souza, A. Tarancón, *J. Phys. Energy* **2022**, *4*, 4.
[9] R. Gao, S. E. Reyes-Lillo, R. Xu, A. Dasgupta, Y. Dong, L. R. Dedon, J. Kim, S. Saremi, Z. Chen, C. R. Serrao, H. Zhou, J. B. Neaton, L. W. Martin, *Chem. Mater.* **2017**, *29*, 6544.
[10] W. Noun, E. Popova, F. Bardelli, Y. Dumont, R. Bertacco, A. Tagliaferri, M. Tessier, M. Guyot, B. Berini, N. Keller, *Phys. Rev. B* **2010**, *81*, 054411.
[11] T. Su, S. Ning, E. Cho, C. A. Ross, *Phys. Rev. Mater.* **2021**, *5*, 094403.
[12] J. Santiso, C. García, C. Romanque, L. Henry, N. Bernier, N. Bagués, J. M. Caicedo, M. Valvidares, F. Sandiumenge, *ChemNanoMat* **2023**, *9*, 202200495.
[13] E. Bousquet, A. Cano, *J. Phys. Condens. Matter* **2016**, *28*, 123001.
[14] J. S. Zhou, L. G. Marshall, Z. Y. Li, X. Li, J. M. He, *Phys. Rev. B* **2020**, *102*, 104420.
[15] R. L. White, *J. Appl. Phys.* **1969**, *40*, 1061.
[16] Y. Tokunaga, N. Furukawa, H. Sakai, Y. Taguchi, T. H. Arima, Y. Tokura, *Nat. Mater.* **2009**, *8*, 558.
[17] Y. Tokunaga, Y. Taguchi, T. H. Arima, Y. Tokura, *Nat. Phys.* **2012**, *8*, 838.
[18] K. F. Wang, J. M. Liu, Z. F. Ren, *Adv. Phys.* **2009**, *58*, 321.
[19] S. Ning, A. Kumar, K. Klyukin, E. Cho, J. H. Kim, T. Su, H. S. Kim, J. M. LeBeau, B. Yildiz, C. A. Ross, *Nat. Commun.* **2021**, *12*, 4298.
[20] A. Kumar, K. Klyukin, S. Ning, C. Ozsoy-Keskinbora, M. Ovsyanko, F. van Uden, R. Krijnen, B. Yildiz, C. A. Ross, J. M. LeBeau, *Adv. Funct. Mater.* **2021**, *32*, 2107017.
[21] A. Kumar, S. Ning, T. Su, E. Cho, J. M. LeBeau, C. A. Ross, *Adv. Electron. Mater.* **2022**, *8*, 2200036.
[22] U. Chowdhury, S. Goswami, D. Bhattacharya, J. Ghosh, S. Basu, S. Neogi, *Appl. Phys. Lett.* **2014**, *105*, 052911.
[23] U. Chowdhury, S. Goswami, D. Bhattacharya, A. Midya, P. Mandal, *Appl. Phys. Lett.* **2016**, *109*, 092902.
[24] U. Chowdhury, S. Goswami, A. Roy, S. Rajput, A. K. Mall, R. Gupta, S. D. Kaushik, V. Siruguri, S. Saravanakumar, S. Israel, R. Saravanan, A. Senyshyn, T. Chatterji, J. F. Scott, A. Garg, D. Bhattacharya, *Phys. Rev. B* **2019**, *100*, 195116.
[25] Y. Ahn, J. Jang, J. Y. Son, *Appl. Phys. A* **2016**, *122*, 531.
[26] X. Yuan, Y. Tang, Y. Sun, M. Xu, *J. Appl. Phys.* **2012**, *111*, 053911.
[27] P. Barrozo, D. R. Småbråten, Y. L. Tang, B. Prasad, S. Saremi, R. Ozgur, V. Thakare, R. A. Steinhardt, M. E. Holtz, V. A. Stoica, L. W. Martin, D. G. Schlom, S. M. Selbach, R. Ramesh, *Adv. Mater.* **2020**, *32*, 2000508.
[28] S. M. Disseler, J. A. Borchers, C. M. Brooks, J. A. Mundy, J. A. Moyer, D. A. Hillsberry, E. L. Thies, D. A. Tenne, J. Heron, M. E. Holtz, J. D. Clarkson, G. M. Stiehl, P. Schiffer, D. A. Muller, D. G. Schlom, W. D. Ratcliff, *Phys. Rev. Lett.* **2015**, *114*, 217602.
[29] S. Song, H. Han, H. M. Jang, Y. T. Kim, N. S. Lee, C. G. Park, J. R. Kim, T. W. Noh, J. F. Scott, *Adv. Mater.* **2016**, *28*, 7430.
[30] T. Katayama, Y. Hamasaki, S. Yasui, A. Miyahara, M. Itoh, *Thin Solid Films* **2017**, *642*, 41.
[31] D. V. Mamedov, T. P. Gavrilova, I. V. Yatsyk, I. F. Gilmutdinov, Z. Y. Seidov, M. A. Aljanov, M. J. Najafzade, I. N. Ibrahimov, V. I. Chichkov, N. V. Andreev, E. Y. Koroleva, R. M. Eremina, *J. Phys.: Conf. Ser.* **2017**, *903*, 012014.
[32] R. C. Rai, D. Mckenna, C. Horvatits, J. Du Hart, *Proc. 12th Pacific Rim Conf. Ceram. Glas. Technol.* (Eds: D. Singh, M. Fukushima, Y. Kim, K. Shimamura, N. Imanaka, T. Ohji, J. Amoroso, M. Lanagan), Wiley, Hoboken, NJ **2018**.
[33] M. S. Vijaya Kumar, K. Kuribayashi, K. Kitazono, *J. Mater. Res.* **2008**, *23*, 2996.
[34] M. Davis, M. Budimir, D. Damjanovic, N. Setter, *J. Appl. Phys.* **2007**, *101*, 054112.

[35] J. L. Zhao, H. X. Lu, J. R. Sun, B. G. Shen, *Phys. B Condens. Matter* **2012**, *407*, 2258.

[36] K. P. Kelley, D. E. Yilmaz, L. Collins, Y. Sharma, H. N. Lee, D. Akbarian, A. C. T. Van Duin, P. Ganesh, R. K. Vasudevan, *Phys. Rev. Mater.* **2020**, *4*, 24407.

[37] D. A. Kiselev, M. S. Afanasiev, S. A. Levashov, A. A. Sivov, G. V. Chucheva, *Thin Solid Films* **2016**, *619*, 214.

[38] Z. Gao, S. Lyu, H. Lyu, *J. Semicond.* **2022**, *43*, 014102.

[39] S. Saremi, R. Xu, L. R. Dedon, J. A. Mundy, S. L. Hsu, Z. Chen, A. R. Damodaran, S. P. Chapman, J. T. Evans, L. W. Martin, *Adv. Mater.* **2016**, *28*, 10750.

[40] X. Qi, J. Dho, R. Tomov, M. G. Blamire, J. L. MacManus-Driscoll, *Appl. Phys. Lett.* **2005**, *86*, 062903.

[41] S. Y. Yang, L. W. Martin, S. J. Byrnes, T. E. Conry, S. R. Basu, D. Paran, L. Reichertz, J. Ihlefeld, C. Adamo, A. Melville, Y. H. Chu, C. H. Yang, J. L. Musfeldt, D. G. Schlom, J. W. Ager, R. Ramesh, *Appl. Phys. Lett.* **2009**, *95*, 93.

[42] H. Matsuo, Y. Kitanaka, R. Inoue, Y. Noguchi, M. Miyayama, *J. Appl. Phys.* **2015**, *118*, 114101.

[43] H. Matsuo, Y. Kitanaka, R. Inoue, Y. Noguchi, M. Miyayama, *Appl. Phys. Lett.* **2016**, *108*, 032901.

[44] Y. Noguchi, H. Matsuo, Y. Kitanaka, M. Miyayama, *Sci. Rep.* **2019**, *9*, 4225.

[45] M. Kohli, P. Muralt, N. Setter, *Appl. Phys. Lett.* **1998**, *72*, 3217.

[46] G. Kresse, J. Furthmüller, *Comput. Mater. Sci.* **1996**, *6*, 15.

[47] G. Kresse, D. Joubert, *Phys. Rev. B* **1999**, *59*, 1758.

[48] J. P. Perdew, K. Burke, M. Ernzerhof, *Phys. Rev. Lett.* **1996**, *77*, 3865.

[49] L. Wang, T. Maxisch, G. Ceder, *Phys. Rev. B* **2006**, *73*, 195107.

[50] A. Jain, G. Hautier, S. P. Ong, C. J. Moore, C. C. Fischer, K. A. Persson, G. Ceder, *Phys. Rev. B* **2011**, *84*, 045115.

[51] O. Kubaschewski, C. B. Alcock, P. J. Spencer, *Materials Thermochemistry*, Pergamon Press, Oxford, UK **1993**.